Phase change in a three-dimensional rectangular cavity under electromagnetically simulated low-gravity

Side wall heating

Douglas L. Veilleux
Raytheon Company, Integrated Defense Systems, Portsmouth, Rhode Island, USA

Eduardo Gonçalves and Mohammad Faghri
Department of Mechanical Engineering, University of Rhode Island, Kingston, Rhode Island, USA

Yutaka Asako
Department of Mechanical Engineering, Tokyo Metropolitan University, Tokyo, Japan, and

Majid Charmchi
Department of Mechanical Engineering, University of Massachusetts, Lowell, Massachusetts, USA

Abstract

Purpose – To demonstrate, through numerical models, that it is possible to simulated low-gravity phase change (melting), of an electrically conducting material (gallium), in terrestrial conditions via the application of electromagnetic fields.

Design/methodology/approach – A complete three-dimensional mathematical formulation governing a phase change process in the presence of an electromagnetic field has been developed. In addition a comprehensive parametric study has been completed to study the various effects of gravity, Stefan number, Hartmann number and electromagnetic pressure number upon the phase change process.

Findings – The results show that the application of an electromagnetic filed can be used to simulate key melting characteristics found for actual low-gravity. However, the resulting three-dimensional flow field in the melted region differs from actual low-gravity. The application of an electromagnetic field creates a flow phenomenon not found in actual low-gravity or previously seen in two-dimensional problems.

Research limitations/implications – Future work may include the use of oscillating electromagnetic fields to enhance convection in energy storage systems in a low-gravity environment.

Practical implications – The ability to suppress unwanted convective flows in a phase change process without the high magnetic fields necessary in magnetic field only suppression systems.

Originality/value – This work fills a void in the literature related to conducting fluids and the effects of magnetic and electromagnetic fields.

Keywords Magnetohydrodynamics, Electromagnetic fields, Numerical analysis

Paper type Research paper

Nomenclature

A = area (m^2)
B_o = externally applied magnetic field (Tesla)
C = specific heat (J kg^{-1} K^{-1})
e = enthalpy function (J kg^{-1})
E = dimensionless enthalpy (defined in equation (32b))
$\mathbf{E}$ = applied electric field (mV)
f_s = solid volume fraction
f_σ = electrical conductivity control parameter
f_μ = viscosity control parameter
g = gravity acceleration (m s^{-2})
g_o = gravity acceleration on earth (m s^{-2})
Gr = Grashoff number (defined in equation (32c))
Ha = Hartmann number (defined in equation (32d))
H' = Joule heating (defined in equation (9))
H^* = heights of container and PCM (m)
h = latent heat (J kg^{-1})
$\mathbf{J}$ = electrical current density (A m^{-2})
L' = dimensionless heat capacity (defined in equation (32d))
L^* = length of container and PCM (m)
Mp = electromagnetic pressure number (defined in equation (32e))
k = thermal conductivity (W m^{-1} K^{-1})
Pr = Prandtl number (defined in equation (32b))
p = pressure field (N m^{-2})
p' = total pressure field (N m^{-2})
P' = dimensionless pressure field (defined in equation (32b))
Re_m = magnetic Reynolds number ($Re_m = \mu_m \sigma u H^*$)
S = dimensionless enthalpy source term
X_{inf} = interface front
Ste = Stefan number
T = temperature (K)
t = time (s)

u, v, w = velocity fields (m s^{-1})
U, V, W = dimensionless velocity fields (defined in equation (32a))
W^* = widths of container and PCM (m)
X, Y, Z = dimensionless coordinates (defined in equation (32a))

Symbols

$\Re$ = electric resistivity
ϕ = electrodynamic scalar potential (volt m^{-1})
α = thermal diffusivity (m^2 s^{-1})
β = coefficient of volumetric expansion (K^{-1})
$\beta_\Re$ = temperature coefficient of resistivity (K^{-1})
σ = electric conductivity (Ω^{-1} m^{-1})
Γ = dimensionless diffusion coefficient
Π_ρ = density ratio (defined in equation (32e))
Π_σ = electric conductivity ratio (defined in equation (32e))
$\Pi_\Re$ = defined in equation (32e)
μ = viscosity (kg m^{-1} s^{-1})
μ_m = magnetic permeability (kg m c^{-2})
ν = kinematic viscosity (m^2 s^{-1})
θ = dimensionless temperature field (defined in equation (32d))
ρ^* = local density (kg m^{-3})
τ = dimensionless time (defined in equation (32b))
ψ = dimensionless electric potential (defined in equation (32b))

Subscripts

o = externally applied
f = fusion (melting)
l = liquid phase
s = solid phase
w = wall

Introduction

The control of natural convective flow during melting and solidification has received significant attention over the past 15 years. With solidification receiving the majority of the attention due to the practical applications (i.e. crystal growth or continuous casting) of controlling convective flows in melted materials. Typically these natural convective induced flows dominate over other induced flows, which may show

contributions at decreased levels of gravity. For example, the expansion or contraction of a solid material undergoing a phase change process can affect the flow field in the melted regions under low-gravity environments (Asako and Faghri, 1999). In the crystal growth industry, the goal is to reduce (if possible eliminate) all the convective flows so that a better end product can be achieved. By controlling (in this case damping) the flow field, a more uniform distribution of impurities can be achieved. Also, the solidification process can proceed in a more conduction-like manner, which can reduce residual stress generated by a liquid forming into a solid. Typically magnetic fields are used to dampen the convective flow in the crystal growth industry. It is well known that a magnetic field can significantly suppress/dampen the convective flow field (Ozoe and Okada, 1989) and thus controlling the solid/liquid interface shape and propagation. Dulikravich *et al.* (1994) confirmed that the strength and the orientation of the magnetic field has profound influence on the solidification and melting since it weakens flow re-circulation regions and causes distorted velocity profiles. However, Dennis and Dulikravich (2002) concluded that velocity within the melt could not be completely halted due to limitations of the applied magnetic field. They postulate that magnetic fields stronger than 1.0 T might be required to completely eliminate motion within the melt.

The study of convective flow suppression in solidification of liquid materials has not been limited to magnetic suppression only, electric and electromagnetic fields have also been applied to control the flow field. Dulikravich and Kosovic (1992) performed a numerical feasibility study examining both magnetic and electric fields independently applied to semi-conducting melts. They concluded that solidification with a strong magnetic filed is significantly slower than solidification in micro gravity, and the application of an electric field caused irregularities in the melt/solid interface shape. Since it is much easier to generate an electric potential field difference than it is to generate a strong magnetic filed, they suggested that the possibility of an optimally controlled solidification process involving magnetic and electric fields may exist. Ha *et al.* (2003) used numerical simulations to compare the thermal flows and solidification of continuous steel casting while under the influence of electromagnetic fields. They concluded that improvements in flow and temperature controls can be obtained by the application of an electromagnetic field. By controlling the temperature field they were able to decrease the maximum and minimum temperature difference and thereby improved uniform quality slab production. Harada *et al.* (1998) concluded that the application of a magnetic field suppresses mixing of solute elements in clad casting. They achieved good correlation between numerical simulation predictions and actual clad casting experiments.

While numerous papers have addressed conducting fluids and the effects of magnetic and electromagnetic fields, none have sought to study the effects of electromagnetic fields on melting when applied and used to simulate low-gravity. It is the aim of this paper to expand the work of Gonçalves *et al.* (2005) into three dimensions and study the resulting effects. Both transverse electric and magnetic fields are used to counteract the gravitational forces exerted on the system during the melting process. The introduction of an electric field can significantly reduce the value of the magnetic field intensity necessary to produce the same Lorentz force needed to counteract the gravitational forces present in the system. However, the flow field distortion is no longer limited to a high magnetic field only as stated by Gonçalves *et al.*

(2005). It is shown that the application of an electromagnetic field generates a flow field phenomenon not present for actual low-gravity. While these distortions in the flow field do exist when an electromagnetic field is applied, it is further shown that the intensity of these distortions is much less than that of an applied magnetic field. Moreover, the results show that an electromagnetic field can be used to better simulate actual low-gravity than a magnetic field alone.

Problem description

The problem geometry consists of a three-dimensional rectangular container of height (H^*), width (W^*), and length (L^*), which houses a solid rectangular phase change material (PCM) (Gallium) of the same size as shown in Figure 1. The entire system is placed under a transverse electromagnetic field. Where the magnetic field is applied in the positive x-direction and is crossed with an electric field in the positive z-direction, thus generating a Lorentz force to oppose the influence of gravity.

Initially the system is kept at the fusion (melting) temperature (T_f). The left sidewall is suddenly raised to a uniform higher temperature ($T_w > T_f$). The right sidewall of the container is kept at the fusion temperature (T_f), and the remaining walls are adiabatic. Melting of the PCM begins and a natural convective flow occurs in the melting region. The front and back walls are electrically conducting while the remaining walls are electrically insulated. The thermophysical and electromagnetic properties associated with the system can be found in Table I.

Governing equations

The melting of an electroconductive PCM in the presence of an electromagnetic field is governed by the conservation of mass, momentum and energy, the induction equations and/or the Poisson equation for electric potential. While this equation set can be solved

Figure 1.
Problem schematic and direction of electric and magnetic fields

Parameter	Symbol	Value	Unit
Width, height, length of PCM	W, H, L	0.04, 0.04, 0.04	m
Melting point	T_m	29.78	°C
Temperature difference	$\Delta T = T_w - T_f$	10.00	°C
Density of solid	ρ_s	5907.0	$kg\,m^{-3}$
Density of melt	ρ_f	6094.7	$kg\,m^{-3}$
Viscosity	μ	1.92×10^{-3}	$kg\,m^{-1}\,s^{-1}$
Thermal conductivity	K	31.24	$W\,m^{-1}\,K^{-1}$
Specific heat (500 K)	C	397.6	$J\,kg^{-1}\,K^{-1}$
Electrical conductivity of solid	σ_s	6644518.0	$mho\,m^{-1}$
Electrical conductivity of melt	σ_f	3846154.1	$mho\,m^{-1}$
Volume coefficient of thermal expansion	β_T	1.27×10^{-4}	K^{-1}
Temperature coefficient of resistivity	$\beta_\Re$	3.12×10^{-3}	K^{-1}
Latent heat of fusion	L	80160.0	$J\,kg^{-1}$
Momentum diffusivity	ν	3.15×10^{-7}	$m^2\,s^{-1}$
Thermal diffusivity of melt	α_f	1.29×10^{-5}	$m^2\,s^{-1}$
Thermal diffusivity of solid	α_S	1.33×10^{-5}	$m^2\,s^{-1}$

Source: Metals Handbook (1990), Filyand and Semenova (1968), and Yahia and Thobe (1972)

Table I.
Electrical and
thermophysical
properties of gallium the
dimension of PCM and
cavity used

numerically it possess significant challenges to obtain a converged solution due to their highly coupled nature. In order to simplify the equation set, the *induction-free MHD approximation* is employed (Davidson, 2001). This approximation allows for the induced fields (magnetic and/or electric) to be neglected when the magnetic Reynolds number (Re_m), which is the ratio of magnetic advection to magnetic diffusion, is much less than unity ($Re_m \cong 6.428 \times 10^{-6}$ for this problem). Thus allowing the MHD effects of the imposed fields to be expressed solely through the source terms in the conservation equations.

In addition to the induction-free MHD approximation the flow is assumed to be laminar, incompressible, and the thermophysical properties are constant in each phase (the properties are evaluated at the melting temperature, T_f). Furthermore, the densities of liquid and solid phases are assumed to be the same, $\rho_s = \rho_l = \rho_f$, except for the density that appears in the body force term which gives rise to the force imbalance between the solid and the liquid phases. The formulation is carried out as a single-domain problem, utilizing the enthalpy method developed by Cao and Faghri (1989) where the same conservation equations are used for both the solid and liquid phases, by considering the solid region as a liquid with an infinite viscosity.

Hence, the governing equations for the motion of both phases will be based on those documented in the previous papers (Gonçalves *et al.*, 2005; Asako *et al.*, 2002). Assuming that the induced magnetic fields are negligible compared to the applied field (B_o), and that the resulting Lorentz force due to electromagnetic field works against gravity, the governing equations can be expressed according by the following laws:

Mass conservation:

$$\frac{\partial u}{\partial x} + \frac{\partial v}{\partial y} + \frac{\partial w}{\partial z} = 0 \tag{1}$$

Momentum conservation:

$$x: \quad \rho^*\frac{\partial u}{\partial t} + \rho^* u\frac{\partial u}{\partial x} + \rho^* v\frac{\partial u}{\partial y} + \rho^* w\frac{\partial u}{\partial z} = \nabla(\mu^*\nabla u) - \frac{\partial p}{\partial x} + F_x \quad (2)$$

$$y: \quad \rho^*\frac{\partial v}{\partial t} + \rho^* u\frac{\partial v}{\partial x} + \rho^* v\frac{\partial v}{\partial y} + \rho^* w\frac{\partial v}{\partial z} = \nabla(\mu^*\nabla v) - \frac{\partial p}{\partial y} - \rho^* g_0 + F_y \quad (3)$$

$$z: \quad \rho^*\frac{\partial w}{\partial t} + \rho^* u\frac{\partial w}{\partial x} + \rho^* v\frac{\partial w}{\partial y} + \rho^* w\frac{\partial w}{\partial z} = \nabla(\mu^*\nabla w) - \frac{\partial p}{\partial z} + F_z \quad (4)$$

Energy conservation (enthalpy transformed; Cao and Faghri, 1989):

$$\rho^*\frac{\partial e}{\partial t} + \rho^* u\frac{\partial e}{\partial x} + \rho^* v\frac{\partial e}{\partial y} + \rho^* w\frac{\partial e}{\partial z} = \nabla(\gamma\nabla e) + \nabla^2 s + H' \quad (5)$$

Current conservation law:

$$\nabla \cdot \mathbf{J} = 0 \quad (6)$$

Ohm's law (for moving media):

$$\mathbf{J} = \sigma^*(\mathbf{E} + u \times B_0 i) = \sigma^*\left[E_x i + (E_y + wB_0)j + (E_z - vB_0)k\right] \quad (7)$$

Lorentz force acting on the system

$$\mathbf{F} = \mathbf{J} \times [B_0 i] = \sigma^*\left[(E_z - vB_0)B_0 j - (E_y + wB_0)B_0 k\right] \quad (8)$$

Joule heating due to flow of current through the medium

$$H' = \frac{\mathbf{J}^2}{\sigma^*} = \sigma^*\left[E_x + (E_y + wB_0)^2 + (E_z - vB_0)^2\right] \quad (9)$$

With the introduction of the electrodynamic scalar potential (ϕ), the electric field $\mathbf{E}$ can be expressed as

$$\mathbf{E} = -\nabla\phi \quad (10)$$

which in turns, reforms Ohm's law (equation (7)) as

$$\mathbf{J} = \sigma^*(-\nabla\phi + u \times B_0 i)$$

$$= \sigma^*\left[-\frac{\partial\phi}{\partial x}i + \left(-\frac{\partial\phi}{\partial y} + wB_0\right)j + \left(-\frac{\partial\phi}{\partial z} - vB_0\right)k\right] \quad (11)$$

from equation (11) and the Current conservation law, equation (6), the governing equation for the electrical potential (ϕ) can be determined as

$$\nabla(\sigma^*\nabla\phi) = \nabla \cdot (\sigma^* u \times B_0 i) \quad (12)$$

or in Cartesian coordinate

$$\frac{\partial}{\partial x}\left(\sigma^* \frac{\partial \phi}{\partial x}\right) + \frac{\partial}{\partial y}\left(\sigma^* \frac{\partial \phi}{\partial y}\right) + \frac{\partial}{\partial z}\left(\sigma^* \frac{\partial \phi}{\partial z}\right) = B_o \frac{\partial}{\partial y}(\sigma^* w) - B_o \frac{\partial}{\partial z}(\sigma^* v) \quad (13)$$

The electromagnetic force acting on the medium in the x, y and z directions, can be expressed as

$$F_x = 0 \quad (14)$$

$$F_y = -\sigma^* \frac{\partial \phi}{\partial z} B_o - \sigma^* v B_o^2 \quad (15)$$

$$F_z = \sigma^* \frac{\partial \phi}{\partial y} B_o - \sigma^* w B_o^2 \quad (16)$$

and the joule heating due to flow of current through the medium is given as

$$H' = \frac{\mathbf{J}^2}{\sigma^*} = \sigma^* \left(\frac{\partial \phi}{\partial x}\right)^2 + \sigma^* \left(-\frac{\partial \phi}{\partial y} + w B_o\right)^2 + \sigma^* \left(-\frac{\partial \phi}{\partial z} - v B_o\right)^2 \quad (17)$$

By reducing the gravitational forces on the medium, the hydrostatic pressure within the melt is also affected. In this case, the hydrostatic pressure ($\rho_f g_o y$) is reduced by the electromagnetostatic pressure ($\rho_f g_m y$) such that the "hydro-electromagnetostatic" pressure can be expressed as

$$p_\infty = \rho_f (g_o - g_m) y \quad (18)$$

g_m is the electromagnetostatic acceleration which opposes gravity throughout the medium even before the melting starts, and is given according to Ramo et $al.$ (1994) as

$$g_m = \frac{\sigma_f E_o B_o}{\rho_f} \quad (19)$$

where

$$E_o \approx E_z = -\frac{\partial \phi}{\partial z}$$

is the constant electric field due to the externally applied current along the z-axis given by $\mathbf{J}_o = \sigma^* E_o$. The total pressure p', felt by the fluid, is the sum of the local pressure (p), plus the hydro-electromagnetostatic pressure (p_∞) given as $p' = p + p_\infty$, or

$$p = p' - \rho_f g_o y + \sigma_f E_o B_o y \quad (20)$$

Then the modified pressure gradient becomes

$$-\frac{\partial p}{\partial x} = -\frac{\partial p'}{\partial x} \quad (21)$$

$$-\frac{\partial p}{\partial y} = -\frac{\partial p'}{\partial y} + \rho_f g_o + \sigma_f \frac{\partial \phi}{\partial z} B_o \quad (22)$$

$$-\frac{\partial p}{\partial z} = -\frac{\partial p'}{\partial z} \quad (23)$$

Under this modified pressure field, the y-momentum equation, equation (3), can be recast as:

$$\rho^*\frac{\partial v}{\partial t}+\rho^*u\frac{\partial v}{\partial x}+\rho^*v\frac{\partial v}{\partial y}+\rho^*w\frac{\partial v}{\partial z}=\nabla(\mu^*\nabla v)-\frac{\partial p}{\partial y}-(\rho^*-\rho_f)g_o-(\sigma^*-\sigma_f)$$

$$\times\frac{\partial\phi}{\partial z}B_o-\sigma^*vB_o^2 \tag{24}$$

The gravitational forces in the liquid and the solid regions can then be expressed under Boussinesq approximation as:

$$-(\rho^*-\rho_f)g_o=\begin{cases}-(\rho_l-\rho_f)g_o=\rho_f\beta(T-T_f)g_o & \text{in the liquid region}\\ -(\rho_s-\rho_f)g_o & \text{in the solid region}\end{cases} \tag{25}$$

Likewise, the electrostatic body force affects the liquid and the solid regions differently. Namely, the two expressions can be given as:

$$-(\sigma^*-\sigma_f)\frac{d\phi}{dz}B_o=\begin{cases}\dfrac{\beta_\Re(T-T_f)}{1+\beta_\Re(T-T_f)}\sigma_f\dfrac{\partial\phi}{\partial z}B_o & \text{the liquid region}\\[2ex] -(\sigma_s-\sigma_f)\dfrac{\partial\phi}{\partial z}B_o & \text{in the solid region}\end{cases} \tag{26}$$

where use of electrical resistivity definition $\Re\equiv1/\sigma$ has been made to derive the temperature-dependent electrostatic body force in the liquid region. Like the density, electrical resistivity is usually assumed to vary linearly with temperature as:

$$\Re_L=\Re_f\left[1+\beta_\Re(T-T_f)\right] \tag{27}$$

where $\beta_\Re$ is the temperature coefficient of resistivity of the PCM.

In terms of electrical conductivity, equation (27) is given as:

$$\frac{1}{\sigma_L}=\frac{1}{\sigma_f}\left[1+\beta_\Re(T-T_f)\right] \quad\text{or}\quad \sigma_L=\frac{\sigma_f}{\left[1+\beta_\Re(T-T_f)\right]} \tag{28}$$

Hence, the effects of temperature change on electrical conductivity difference within the liquid region can be expressed as:

$$\sigma_L-\sigma_f=\frac{\sigma_f}{\left[1+\beta_\Re(T-T_f)\right]}-\sigma_f=-\frac{\beta_\Re(T-T_f)\sigma_f}{\left[1+\beta_\Re(T-T_f)\right]} \tag{29}$$

which leads to the outcome of equation (26). Thus the final form of y-momentum can be rewritten as,

$$\rho^* \frac{\partial v}{\partial t} + \rho^* u \frac{\partial v}{\partial x} + \rho^* v \frac{\partial v}{\partial y} + \rho^* w \frac{\partial v}{\partial z} = \nabla(\mu^* \nabla v) - \frac{\partial p'}{\partial y}$$

$$+ \begin{cases} \rho_f \beta (T - T_f) g_o + \dfrac{\beta_{\Re}(T - T_f)}{1 + \beta_{\Re}(T - T_f)} \sigma_f \dfrac{\partial \phi}{\partial z} B_o \\ -(\rho_S - \rho_f) g_o - (\sigma_s - \sigma_f) \dfrac{\partial \phi}{\partial z} B_o \end{cases}$$

$$- \sigma^* v B_o^2$$

$$(30)$$

Note that as with density, the electrical conductivity is assumed constant in each phase, except for the terms in the body force. This is in agreement with the criteria of Boussinesq approximation.

Boundary conditions

$$t \leq 0 \quad u = v = w = 0 \quad \text{and} \quad e = 0 \tag{31a}$$

$$t \geq 0 \quad u = v = w = 0 \quad \text{on all the walls} \tag{31b}$$

$$\begin{aligned} \frac{\partial \phi}{\partial y} &= 0 \quad \text{top and bottom walls} \\ \frac{\partial \phi}{\partial x} &= 0 \quad \text{left and right walls} \\ \phi &= \phi_o \quad \text{back wall} \\ \phi &= \phi_1 \quad \text{front wall} \end{aligned} \tag{31c}$$

$$\begin{aligned} e &= h + C(T_w - T_f) \quad &&\text{on the left wall} \\ e &= 0 \quad &&\text{on the right wall} \\ \frac{\partial e}{\partial y} &= 0 \quad &&\text{on the top and bottom walls} \\ \frac{\partial e}{\partial z} &= 0 \quad &&\text{on the front and back walls} \end{aligned} \tag{31d}$$

Dimensionless parameters
To cast the governing equations in dimensionless form, the following dimensionless group and parameters are used:

$$X = \frac{x}{H^*}, \quad Y = \frac{y}{H^*}, \quad Z = \frac{z}{H^*}, \quad U_{\text{ref}} = \frac{\alpha_{\text{f}}}{H^*}, \quad U = u\frac{H^*}{\alpha_{\text{f}}}, \quad V = v\frac{H^*}{\alpha_{\text{f}}}, \quad W = w\frac{H^*}{\alpha_{\text{f}}} \quad (32a)$$

$$\psi = \frac{\phi - \phi_{\text{l}}}{\phi_0 - \phi_{\text{l}}} = \frac{\phi - \phi_{\text{l}}}{\Delta\phi}, \quad E = \frac{e}{h}, \quad P' = \frac{p'}{\rho_{\text{f}} U_{\text{ref}}^2}, \quad \tau = t\frac{\alpha}{(H^*)^2}, \quad \text{Pr} = \frac{\nu_{\text{f}}}{\alpha_{\text{f}}} \quad (32b)$$

$$Ar = \frac{(\rho_{\text{S}} - \rho_{\text{f}})g_0(H^*)^3}{\rho_{\text{f}}\,\nu_f^2}, \quad Gr = \frac{g_0\beta(T_{\text{w}} - T_{\text{f}})(H^*)^3}{\nu_{\text{f}}}, \quad Ste = \frac{C_{\text{f}}}{h}(T_{\text{w}} - T_{\text{f}}) \quad (32c)$$

$$Ha = B_0\sqrt{\frac{H^{*2}\sigma_{\text{f}}}{\rho_{\text{f}}\nu_{\text{f}}}}, \quad \theta = \frac{(T - T_{\text{f}})}{(T_{\text{w}} - T_{\text{f}})}, \quad S = s\frac{C_{\text{f}}}{hk_{\text{f}}}, \quad L' = \frac{\alpha_{\text{f}}^2}{(H^*)^2 h} \quad (32d)$$

$$\text{Mp} = \frac{\sigma B_0 \Delta\phi(H^*)^3}{\rho_{\text{f}}\nu_{\text{f}}^2}, \quad \Pi_{\Re} = \beta_{\Re}\Delta T, \quad \Pi_{\rho} = \frac{\rho_{\text{s}}}{\rho_{\text{f}}}, \quad \Pi_{\sigma} = \frac{\sigma_{\text{s}}}{\sigma_{\text{f}}} \quad (32e)$$

With the introduction of the aforementioned dimensionless parameters, the governing equations are given as:

Continuity equation:

$$\frac{\partial U}{\partial X} + \frac{\partial V}{\partial Y} + \frac{\partial W}{\partial Z} = 0 \quad (33)$$

X-momentum:

$$\frac{\partial U}{\partial \tau} + U\frac{\partial U}{\partial X} + V\frac{\partial U}{\partial Y} + W\frac{\partial U}{\partial Z} = \nabla(\Gamma_{\mu}\nabla U) - \frac{\partial P'}{\partial X} \quad (34)$$

Y-momentum:

$$\frac{\partial V}{\partial \tau} + U\frac{\partial V}{\partial X} + V\frac{\partial V}{\partial Y} + W\frac{\partial V}{\partial Z} = \nabla(\Gamma_{\mu}\nabla V) - \frac{\partial P'}{\partial Y} + (1 - f_{\text{s}})GrPr^2\Theta$$
$$+ (1 - f_{\text{s}})\frac{\Pi_{\Re}\text{Mp}Pr^2\theta}{1 + \Pi_{\Re}\theta}\frac{\text{d}\psi}{\text{d}Z} - f_{\sigma(\Theta)}Ha^2PrV \quad (35)$$

Z-momentum:

$$\frac{\partial W}{\partial \tau} + U\frac{\partial W}{\partial X} + V\frac{\partial W}{\partial Y} + W\frac{\partial W}{\partial Z} = \nabla(\Gamma_{\mu}\nabla W) - \frac{\partial P'}{\partial Z} + f_{\sigma(\Theta)}\text{Mp}Pr^2\frac{\text{d}\psi}{\text{d}Y}$$
$$- f_{\sigma(\Theta)}Ha^2PrW \quad (36)$$

Electric potential:

$$\frac{\partial}{\partial X}\left(f_{\sigma(\Theta)}\frac{\partial\psi}{\partial X}\right) + \frac{\partial}{\partial Y}\left(f_{\sigma(\Theta)}\frac{\partial\psi}{\partial Y}\right) + \frac{\partial}{\partial Z}\left(f_{\sigma(\Theta)}\frac{\partial\psi}{\partial Z}\right)$$

$$= \frac{Ha^2}{MpPr}\left[\frac{\partial}{\partial Y}(f_{\sigma(\Theta)}W) - \frac{\partial}{\partial Z}(f_{\sigma(\Theta)}V)\right] \tag{37}$$

Energy equation:

$$\frac{\partial E}{\partial \tau} + U\frac{\partial E}{\partial X} + V\frac{\partial E}{\partial Y} + W\frac{\partial E}{\partial Z} = \nabla(\nabla\Gamma_\alpha E) + \nabla^2 S + f_{\sigma(\Theta)}Ha^2 PrL'\left[\left(\frac{MpPr}{Ha^2}\frac{\partial\psi}{\partial X}\right)^2\right.$$

$$\left. + \left(-\frac{MpPr}{Ha^2}\frac{\partial\psi}{\partial Y} + W\right)^2 + \left(-\frac{MpPr}{Ha^2}\frac{\partial\psi}{\partial Z} - V\right)^2\right] \tag{38}$$

where f_s is the solid volume fraction in a control volume, i.e.

$$f_s = \begin{cases} 0 & \text{liquid phase} \\ 0 < f_s < 1, & \text{melting zone} \\ 1 & \text{solid phase} \end{cases} \tag{39}$$

such that, the local density can be expressed as:

$$\rho^* = \rho_f + f_s(\rho_s - \rho_f) \tag{40}$$

the electrical conductance also follows a similar relation as density, i.e.

$$\sigma^* = \sigma_f + f_s(\sigma_s - \sigma_f) \tag{41}$$

which gives rise to the electrical conductivity control parameter as:

$$f_\sigma = \frac{\sigma^*}{\sigma_f} = 1 + f_s(\Pi_\sigma - 1) \tag{42}$$

or if the temperature effect in the liquid region is taken into account then equation (41) can be expressed more generally as

$$f_{\sigma(\Theta)} = \frac{\sigma^*(\Theta)}{\sigma_f} = \frac{1}{1 + \Pi_\Re\Theta} + f_s\left(\Pi_\sigma - \frac{1}{1 + \Pi_\Re\Theta}\right) \tag{43}$$

where Π_σ is the reference solid-to-liquid electric conductivity ratio defined in equations (32a)-(32e).

The viscosity control parameter f_μ is given as:

$$f_m = \begin{cases} 1 & \text{liquid phase} \\ 1 < f_m < \infty, & \text{melting zone} \\ \infty & \text{solid phase} \end{cases} \quad (44)$$

such that the diffusion coefficient in the dimensionless momentum equation can be generalized as:

$$\Gamma_\mu = Prf_\mu \quad (45)$$

The diffusion coefficient (Γ_α), and the source term (S) for the dimensionless energy equation becomes:

$$\Gamma_\alpha = \begin{cases} 1 \\ 0 \\ \alpha_S/\alpha_f \end{cases} \quad \text{and} \quad S = \begin{cases} -1 & \text{in liquid region where} & E \geq 1 \\ 0 & \text{in mushy region where} & 0 < E < 1 \\ 0 & \text{in solid region where} & E \leq 0 \end{cases} \quad (46)$$

Dimensionless initial and boundary conditions

$$t \leq 0 \quad U = V = W = 0 \quad \text{and} \quad E = 0 \quad (47a)$$

$$t \geq 0 \quad U = V = W = 0 \quad \text{on all the walls} \quad (47b)$$

$$\frac{\partial \psi}{\partial Y} = 0 \quad \text{top and bottom walls}$$

$$\frac{\partial \psi}{\partial X} = 0 \quad \text{left and right wall}$$

$$\psi = 1 \quad \text{back wall} \quad (47c)$$

$$\psi = 0 \quad \text{front wall}$$

$$E = 1 + Ste \quad \text{on the left walls}$$

$$E = 0 \quad \text{on the right walls}$$

$$\frac{\partial E}{\partial Y} = 0 \quad \text{on the top and bottom walls} \quad (47d)$$

$$\frac{\partial E}{\partial Z} = 0 \quad \text{on the front and back walls}$$

Numerical procedure

The governing equations (33)-(38) were discretized using a control-volume based finite difference scheme. The SIMPLE algorithm (Patankar, 1980) was used to solve the coupled heat transfer and magnetohydrodynamic (MHD) flow problem. The QUICK scheme of Hayase *et al.* (1992) coupled with a modified upwind method proposed by Cao and Faghri (1989), was employed in the solution of the dimensionless enthalpy

equation. An upwind scheme was used for the solution of the potential equation and a power law scheme was utilized for the remaining discretized momentum equations.

The grid dependence was examined for a series of three-dimensional grid systems. The mass circulation and solid/liquid interface location, taken at the center of the enclosure and points along the enclosure boundaries, for the different grid systems are presented in Table II and Figure 2. The difference between the $62 \times 40 \times 31$ and the $42 \times 42 \times 22$ grid system for the mass circulation is 1.99 percent. The difference between the aforementioned grid systems for the interface locations (Table II) (jm, kb), (jm, km), (jm, kf), (jb, km), and (jt, km) is 0.22, 0.22, 0.22, 0.05, and 0.11 percent, respectively. Since the difference between these systems was very small it was decided to continue the remaining simulations at $42 \times 42 \times 22$ while at the same time realizing the benefit of decreased computational time.

With the grid dependence study completed the effects of the time step were then examined. Time steps of 0.01, 0.001 and 0.0001 were studied. Because of its coarse size the 0.01 time step cause difficulty in obtaining convergence and was subsequently eliminated from consideration. The difference in the calculated mass circulation for the 0.001 and 0.0001 time steps was 0.22 percent, with an increase in run time of 400 percent for the 0.0001 time step and, therefore, it was decided to perform all calculations at a time step of 0.001.

Finally the problem convergence was controlled by the residual term calculated during each iteration. A maximum residual of 1.0×10^{-6} is used to determine the problem convergence and time step advancement. When the discretized governing equations (34)-(38) are evaluated for convergence, every cell within the domain must contain a residual of less than 1.0×10^{-6}.

| | | Interface location (X_{inf}) | | | | | |
Grid system	Mass circulation (ψ_{max})	(jm, kb)	(jm, km)	(jm, kf)	(jb, km)	(jt, km)	Run time (min)
$22 \times 22 \times 22$	0.58214	0.62695	0.62695	0.62695	0.60873	0.65663	17
$32 \times 32 \times 32$	0.61201	0.62766	0.62766	0.62766	0.60800	0.65589	334
$42 \times 42 \times 22$	0.63161	0.62821	0.62821	0.62821	0.60662	0.65747	374
$42 \times 42 \times 42$	0.63453	0.62768	0.62768	0.62768	0.60744	0.65533	774
$52 \times 52 \times 52$	0.64689	0.62684	0.62684	0.62684	0.60706	0.66000	2,413
$62 \times 40 \times 31$	0.64446	0.62682	0.62682	0.62682	0.60628	0.65676	1,003

Table II.
Grid dependence study
($Pr = 0.0244$,
$Gr = 80358.46$, $\tau = 4$)

Notes:
jb=enclosure bottom (Y-axis)
jm=enclosure middle (Y-axis)
jt=enclosure top (Y-axis)
kb=enclosure back (Z-axis)
km=enclosure middle (Z-axis)
kf=enclosure front (Z-axis)
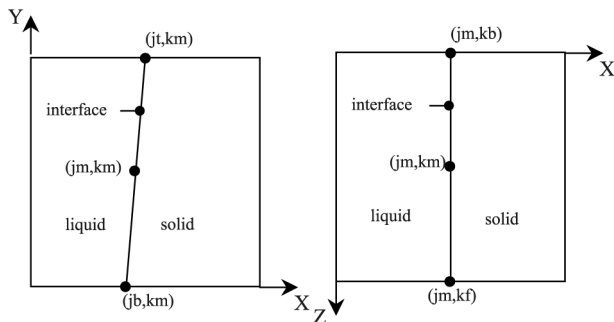
Figure 2.
Position references

Code validation

In order to validate the accuracy of the computer code two test cases were performed. The first test case consisted of a natural convection problem with and without the application of a magnetic field in the x-direction. For this the work of Bessaih *et al.* (1999) was used as a benchmark. Their problem consisted of a cubical enclosure filled with liquid gallium subjected to a temperature differential in the x-direction. A grid system similar to that of Bessaih *et al.* (1999) was utilized for our code validation. A parametric study was performed where the Rayleigh (Ra) number was varied from 10^4 to 10^6 and the magnetic field (Ha) in the x-direction was varied from zero to 100, all for $Pr = 0.025$. The identical boundary conditions have been used where the hot wall is maintained at $\theta = 1.0$ and the cold wall is maintained at $\theta = 0$. The average Nusselt number (Nu) calculated on the hot wall can be seen over laying the results of Bessaih *et al.* (1999) in Figure 3. As seen the results show good agreement with the literature.

The second test case examined was a solidification problem with and without the presence of a magnetic field in the x-direction. For this the work of Dulikravich *et al.* (1994) was used as a benchmark. One of their problems consisted of a cubical enclosure filled with molten silicon subjected to a temperature differential in the x-direction. A grid system of $20 \times 20 \times 20$, similar to that of Dulikravich *et al.* (1994), was utilized for our code validation. They presented results for $Gr = 67.99 \times 10^4$, $Pr = 0.01161$, and $Ha = 0$ and 100. Since they examined a solidification problem they were primarily concerned with the amount of solid which accrued over time. To track this accrued solid they calculated the number of solidified cells within the computation domain. A solidified cell consists of a discretized volume of the computation domain which has been completely solidified from melted material. Two numerical runs were performed, the first without a magnetic field and the second with a magnetic field ($Ha = 100$)
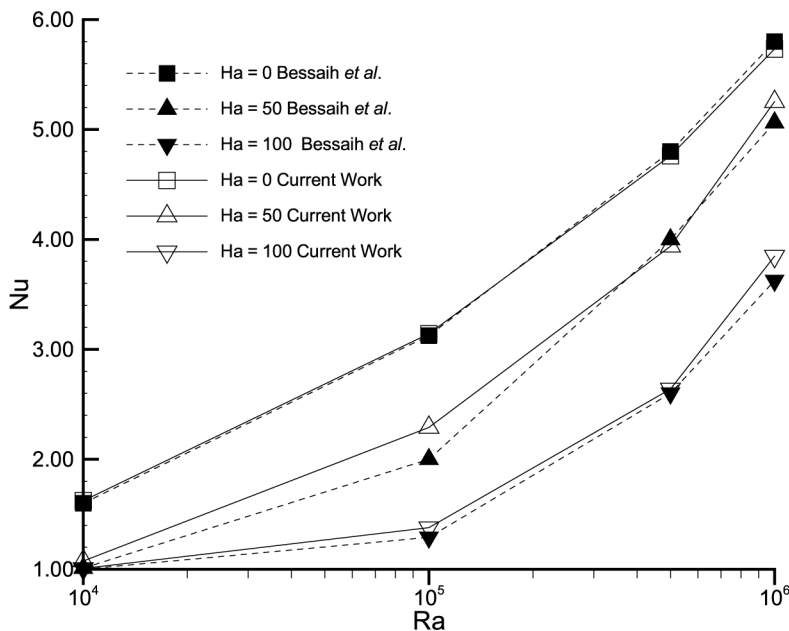
Figure 3.
Variation of the average Nusselt number as a function of *Ra*, *Ha*: solid geometries are from Bessaih *et al.* (1999) and hollow geometries are from current work

applied in the x-direction. The identical boundary conditions have been used where the hot wall is maintained at $\theta = 2.0$ and the cold wall is maintained at $\theta = -1.0$. For the case where no magnetic field has been applied, a comparison of the number of solidified cells showed a reasonable variation of 5.3 percent (1,761 cells vs 1,666 cells) over the test case results. For the case where a magnetic field was applied, a comparison of the number of solidified cells resulted in a 1.6 percent increase (2,020 cells vs 1,986 cells) over the test case results.

Discussion of results

Low-gravity can be simulated by an electromagnetic field in one of the following configurations:

- low electric field and a high magnetic field;
- low magnetic field and an high electromagnetic field; and
- everything in between.

Owing to the countless possible combinations, all efforts will be concentrated on the two limiting cases. We will refer to the "Low electric field with high magnetic field" as the magnetic simulation of low-gravity or "magnetic low-g", and the "Low magnetic field with high electric field" as the electromagnetic simulation of low-gravity or "electromagnetic low-g". The governing parameters for each case are the Hartmann number (Ha), for magnetic low-g, and the electromagnetic pressure number (Mp), for electromagnetic low-g.

In order to simulate low-gravity via an electromagnetic field, the correct field strength must be determined such that the Lorentz force associated with this field can be used to damp and/or counter act the effects of normal gravity. By studying the effects of low-gravity, magnetic, and electromagnetic fields on the mass circulation (ψ_{max}) a correlation between low-gravity and simulated low-gravity has been developed (Figure 4). The mass circulation represents the mass flow of melted PCM passing through an imaginary plane in the XZ plane located at $Y = 0.5$ and can be defined as $\psi_{max} = \rho_l v A$ where ρ_l, v, and A are the liquid density, liquid velocity and area, respectively.

The computations were first carried out for actual low-gravity where both fields are set to zero (i.e. $Ha = Mp = 0$) and the Grashoff number (Gr) is the controlling parameter which is a function of the gravity acceleration. The gravity acceleration has been varied from $9.81 \, \mathrm{m\,s^{-2}}$ to $0.00000981 \, \mathrm{m\,s^{-2}}$ and the ratio of the gravity acceleration (g) to normal gravity (g_o) is used to classify the level of low-gravity (i.e. $g/g_o = 0.0981/9.81 = 10^{-2}$ is referred as 10^{-2} level of low-gravity). The resulting data was plotted (the line with hollow squares) on a reverse Gr-axis so that at normal gravity, the $\psi_{max}(Gr)$ curve coincides with those of zero-field (i.e. $\psi_{max}(Gr_o) = \psi_{max}(Ha = 0) = \psi_{max}(Mp = 0)$), where $Gr_o = Gr(g_o)$ and g_o is the normal gravity. Next the effects of a varying magnetic field were studied with the gravitational level set to Gr_o (normal gravity) and $Mp = 0$ (no applied electric field). The resulting data was plotted in terms of Hartman number (Ha) and is depicted by the line with hollow circles in Figure 4. Finally, the effects of a varying electromagnetic field were studied with the gravity level set to Gr_o (normal gravity). To do so, a relatively weak ($B = 0.01 \, \mathrm{T}$) fixed magnetic field is crossed with a varying electric field. The value of $B = 0.01 \, \mathrm{T}$ was the weakest magnetic field (by order of magnitude),
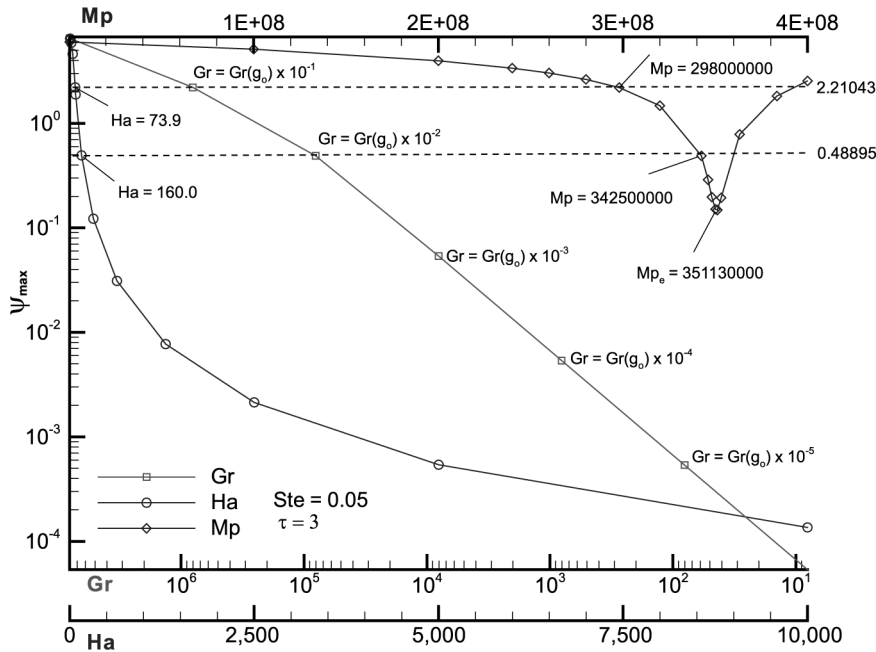
Figure 4.
Mass circulation as a
function of gravity
(hollow squares), magnetic
low-gravity
(hollow circles), and
electromagnetic
low-gravity
(hollow diamonds) at
$\tau = 3$ and $Ste = 0.05$

necessary to prevent the effects of Joule heating from setting in. The subsequent data
was plotted in terms of electromagnetic pressure (Mp) and is depicted by the line with
hollow diamonds. The values of $Ha(\mathbf{B})$ and $Mp(\Delta\phi)$ necessary to simulate low-gravity
can be attained by matching the mass circulation (ψ_{max}) in a straight line across the
three curves. The ranges and values for selected cases of simulated low-gravity are
presented in Table III.

Upon examination of Figure 4, the limitations of simulating low-gravity via
magnetic and electromagnetic fields are evident. For the magnetic field simulations, the
$\psi_{max}(Ha)$ curve displays an asymptotic behavior suggesting that an infinitely large
magnetic field is required to achieve a true zero-g environment. For the electromagnetic
filed simulation, the $\psi_{max}(Mp)$ curve shows that a zero-g environment cannot be
achieved under any circumstances. Furthermore, it is apparent that a critical value of
electromagnetic pressure (Mp_e) exists for which the flow behavior changes abruptly
and actually reverses in flow direction. The details of this anomaly will be discussed in
detail further along in this paper.

Low-gravity		Simulation via electromagnetic field			Simulation via magnetic field		
g/g_o	$Gr(g)$	$\Delta\phi(V)$	Mp $(0.01, \Delta\phi)$		B_o (T)	Ha	**Table III.**
10^{-1}	8035845.80	4.090×10^{-5}	289,000,000		0.0413	73.9	Low-gravity range and its equivalent in magnetic
10^{-2}	803584.580	4.658×10^{-5}	342,500,000		0.0894	160.0	and electromagnetic simulation

A comparative analysis has been performed, using the results of Tables III and IV, between the low-gravity and simulated low-gravity cases to study the three-dimensional effects on the flow field and interface shape along with key melting characteristics such as the interface location (X_{inf}), and melt rate (DV/DV_0). Furthermore, each of these characteristics was analyzed with respect to the effects of gravity levels and Stefan number as curve parameters.

Three-dimensional effects
The interface shapes and velocity vector fields are shown in Figures 5-7. As shown in Figures 5-7, labels (a), (b), and (c) represents true low-gravity, electromagnetically simulated low-gravity and magnetically simulated low-gravity, respectively. While the labels (0), (1) and (2) represents the gravity level for which case, (0) corresponds to natural convection or $g = g_o$, with $Ha = Mp = 0$, (1) corresponds to $g/g_o = 10^{-1}$ with simulation by magnetic field given as $Ha = 73.9$ and by electromagnetic field as $Mp = 298,000,000$ and finally, label (2) corresponds to $g/g_o = 10^{-2}$ with simulated case given by $Ha = 160.0$ and $Mp = 342,500,000$.

Figure 5 shows the XY plane located at $Z = 0.5$ for natural convection, low-gravity and simulated low-gravity at $\tau = 3$ and $Ste = 0.05$. It can be seen that the effects of natural convection decrease dramatically by reducing the level of gravity by only two orders of magnitude. Comparison of the flow field and interface shape (solid line) shows good agreement between that of true low-gravity and electromagnetically simulated low-gravity. However, this is not the case for magnetically simulated low-gravity. The flow field is distorted for all cases that a magnetic field is used to dampen or suppress the convective flow. The effect of the magnetic field (B_o) suppresses motion normal to the field while enhancing it parallel to the field (Gonçalves *et al.*, 2005; Hayase *et al.*, 1992). By inspection of Figures 7(c1) and (c2) a "squeezing" of the flow to the walls and interface front can be observed which is a direct result of the know behavior of a conducting fluid subjected to a magnetic field. This "squeezing" effect forms what is commonly called the Hartman layer.

Figure 6 shows the XZ plane located at $Y = 0.5$ for natural convection, low-gravity and simulated low-gravity at $\tau = 3$ and $Ste = 0.05$. Examination of this plane and the YZ plane (discussed further along) is where the true three-dimensional nature of this problem begins to show. For the natural convection case and the $g/g_o = 10^{-1}$ case some interesting observations can be made:

Dimensionless parameters	Symbol	Value
Aspect ratio	A	1.00
Grashoff number	Gr	8099090.44
Electromagnetic pressure number	Mp	266894896.64
Hartmann number	Ha	1790.29
Phase transition number	L'	1.296×10^{-12}
Prandtl number	Pr	0.024
Stefan number	*Ste*	0.05
Electrical conductivity ratio	Π_σ	1.73
Thermal diffusivity ratio	Π_α	1.03
Dimensionless resistivity	$\Pi_\Re$	0.031

Table IV.
Dimensionless parameters and their characteristic values
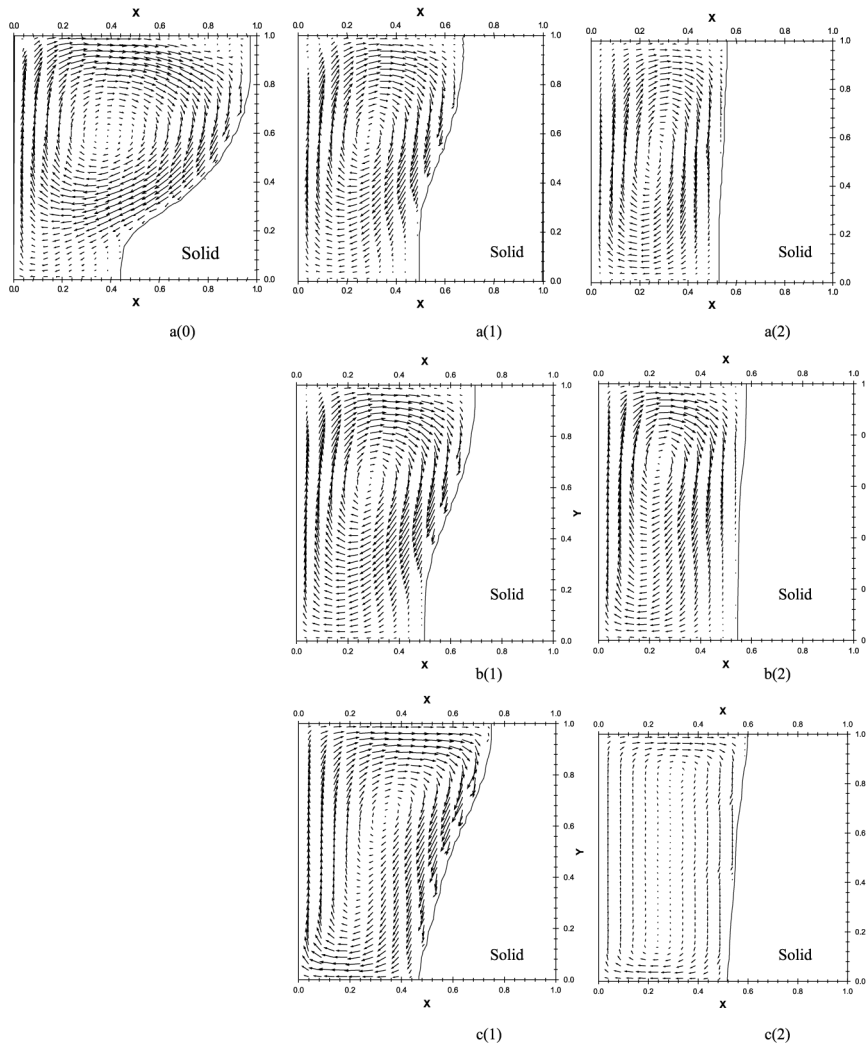
Figure 5.
Interface shape and
velocity vectors in the XY
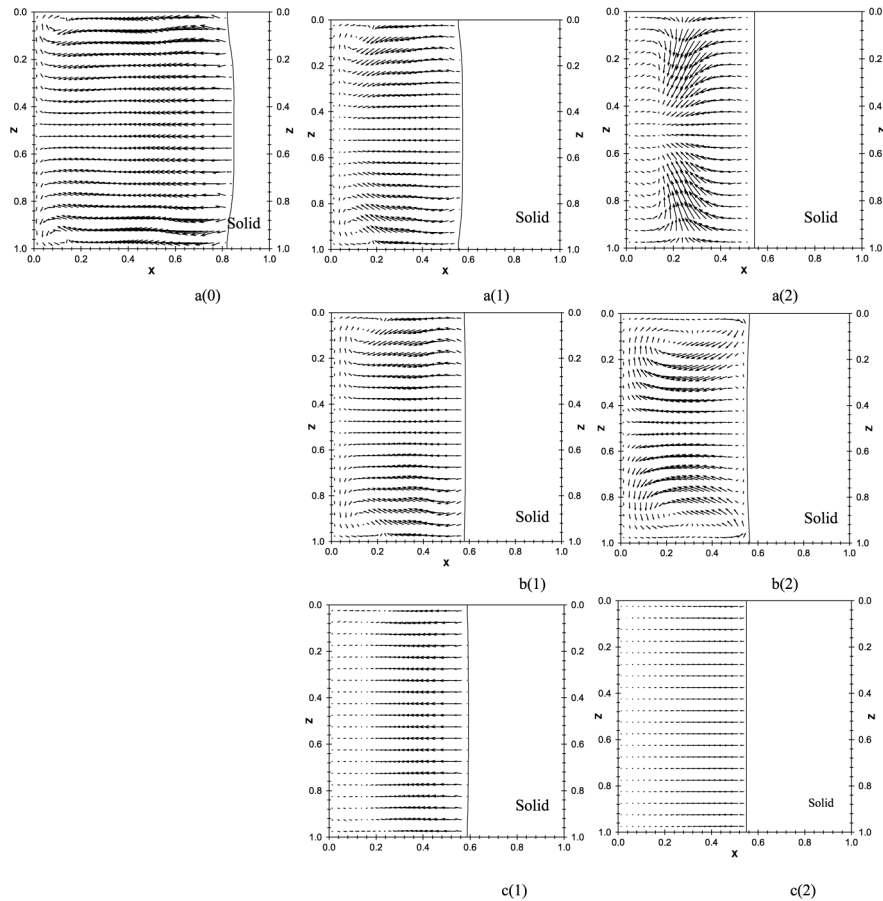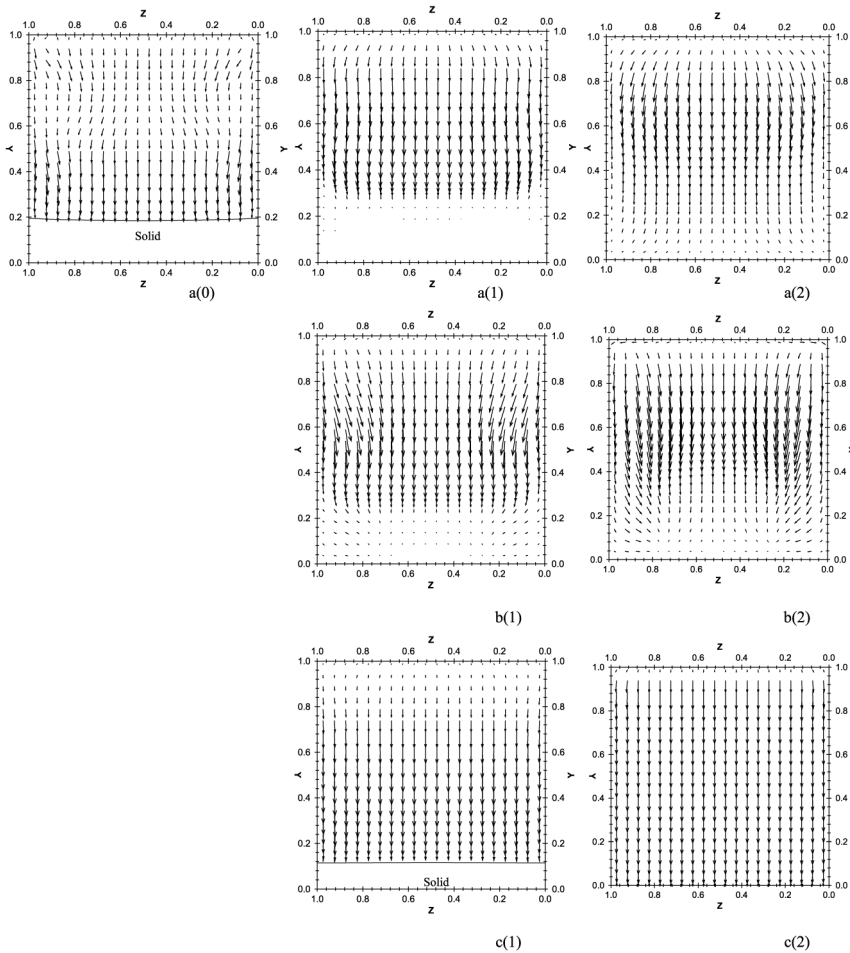plane ($Z = 0.5$) at $\tau = 3$
and $Ste = 0.05$

Notes: (a) Actual Low Gravity, (b) Electromagnetically Simulated Low Gravity,
(c) Magnetically Simulated Low Gravity: (0) Natural Convection, (1) $g/g_0 = 10^{-1}$,
Mp = 2.98 x10^8, Ha = 73.9, (2) $g/g_0 = 10^{-2}$, Mp = 3.39 x10^8, Ha = 160.0

- a "scalloping" effect is occurring which causes the interface front to have a
  concave shape in addition to the natural convective shape shown in Figure 5; and
- a symmetry appears to form about the XY plane at $Z = 0.5$.

These distortions in the flow field and interface shape are a direct result of the interface
front moving with time and the no slip boundary conditions at the enclosure walls. For
the $g/g_o = 10^{-2}$ case the decrease in the level of gravity has a significant effect on the

Notes: (a) Actual Low Gravity, (b) Electromagnetically Simulated Low Gravity,
(c) Magnetically Simulated Low Gravity: (0) Natural Convection, (1) $g/g_0 = 10^{-1}$,
Mp = 2.98 x10^8, Ha = 73.9, (2) $g/g_0 = 10^{-2}$, Mp = 3.39 x10^8, Ha = 160.0

interface shape along with the flow field. The interface straightens out due to the
reduced intensity of the buoyancy forces driving the fluid flow. Comparison of the flow
field and interface shape show that the electromagnetically simulated low-gravity
compares quite well for the $g/g_o = 10^{-1}$ case. It can be seen that the interface shape
still contains a slight "scalloping" effect and the flow field contains re-circulation cells
in the upper and lower left hand corners of the enclosure. As the electromagnetic field
was increased to simulate the $g/g_o = 10^{-2}$ case the flow field and interface shape
begin to change from that of actual low-gravity. The re-circulation cells present for
$g/g_o = 10^{-1}$ case have intensified and as a direct result have caused the interface
shape to become slightly convex. Again the magnetically simulated low-gravity does
not compare well to that of actual low-gravity as expected from the previous
discussion. Only for the $g/g_o = 10^{-2}$ case, where the problem becomes conduction like,

does the interface shape appear in agreement with true low-gravity. However, the flow field is significantly distorted from actual low-gravity.

Figure 7 shows the YZ plane located at $X = 0.5$ for natural convection, low-gravity and simulated low-gravity at $\tau = 3$ and $Ste = 0.05$. In this plane the results show, as expected, that the magnetically simulated flow field and interface shape are distorted from actual low-gravity. The electromagnetically simulated low-gravity appears similar for the $g/g_o = 10^{-1}$ case but differ from the $g/g_o = 10^{-2}$ case. Upon examination of Figure 7 for the $g/g_o = 10^{-2}$ case, it can be seen that the flow fields for both actual low-gravity and electromagnetically simulated low-gravity contains a symmetry plane. But the flow fields are opposite of each other about this symmetry

Notes: (a) Actual Low Gravity, (b) Electromagnetically Simulated Low Gravity, (c) Magnetically Simulated Low Gravity: (0) Natural Convection, (1) $g/g_0 = 10^{-1}$, Mp = 2.98 x10^8, Ha = 73.9, (2) $g/g_0 = 10^{-2}$, Mp = 3.39 x10^8, Ha = 160.0
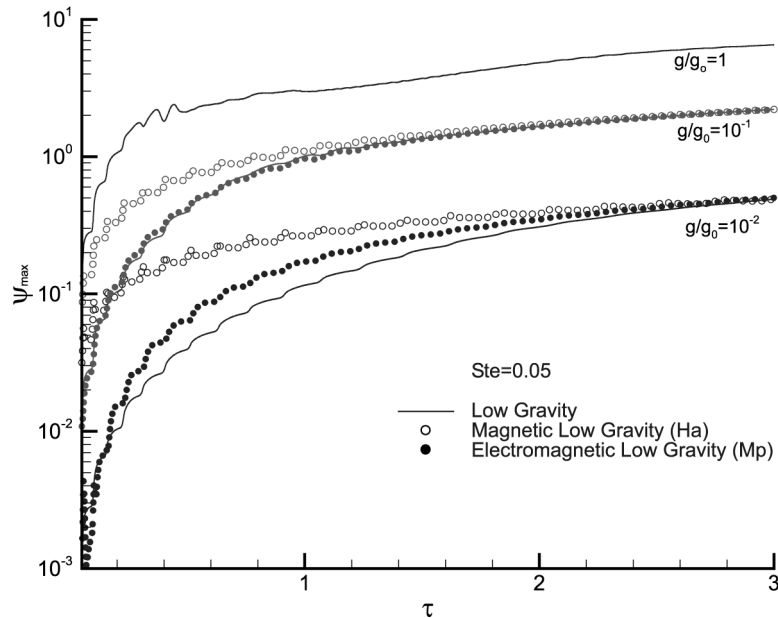
Figure 7.
Interface shape and velocity vectors in the YZ plane ($X = 0.5$) at $\tau = 3$ and $Ste = 0.05$

plane. For actual low-gravity the flow field curves away from the symmetry plane at the top of the enclosure and then straightens out at the middle of the enclosure before curving slightly away from the symmetry plane again at the bottom. However, for electromagnetically simulated low-gravity the flow field curves in towards the symmetry plane at the top of the enclosure and then straightens out at the middle of the enclosure before curving back inward toward the symmetry plane at the bottom of the enclosure.

Mass circulation
The mass circulation (ψ_{max}) as a function of dimensionless time is shown in Figure 8 for both actual low-gravity and simulated low-gravity. It can be seen that the curves converge at $\tau = 3$ which is the time where the graphical correlation was obtained. The electromagnetically simulated low-gravity (solid circles) shows excellent agreement with the $g/g_o = 10^{-1}$ case of low-gravity (solid lines). The $g/g_o = 10^{-2}$ case of electromagnetically simulated low-gravity does not compare as well as the $g/g_o = 10^{-1}$ case. This can be directly attributed to the following. The level of Mp required to achieve the $g/g_o = 10^{-2}$ case is very close to the level in which the flow reverses direction, Mp_e and can be seen in Figure 4. Because this level of low-gravity is close to the reversal point, the buoyancy forces created by the temperature gradient do not dominate the flow field, causing the mass circulation diverge slightly. Furthermore, the three-dimensional effects caused by the application of an electromagnetic field have intensified in strength and are also influencing the mass circulation.

As an aside it should be noted that when using an electromagnetic field to simulate low-gravity to levels greater than $g/g_o = 10^{-1}$ it is necessary to increase the grid density in the z-direction in order to capture the three-dimensional effects on the mass

Figure 8.
Effect of gravity level on the mass circulation (ψ_{max}) as a function of time

circulation. For the $g/g_o = 10^{-2}$ case, a grid system of $42 \times 42 \times 42$ was utilized to capture the aforementioned effects on the mass circulation. Upon further examination it was determined that the mass circulation is the only parameter of this study to have a significant dependency on the grid density in the z-direction. This can be seen in Figures 9(a)-(c), where the interface location (X_{inf}), mass circulation (ψ_{max}), and melt rate have been plotted for various grid systems. The interface location and melt rate, showed no significant variation in value with increased grid density in the z-direction.

For magnetically simulated low-gravity (hollow circles), significant disagreement exists with that of actual low-gravity, which is expected from the known behavior of a conducting fluid in the presence of a magnetic field (Asako and Faghri, 1999).

Interface location
The characteristics of this problem are such that the interface location is a good measure of melting for the fixed PCM, because at low-gravity conditions the processes essentially becomes conduction-like as shown in Figure 5. The interface location is presented at the middle of the Y- and Z-axes. Figure 10 shows the interface location as a function of time for actual low-gravity and simulated low-gravity. Figure 10(a) shows the effects of gravitational level on the interface location, where the results show that the interface location for both magnetically and electromagnetically simulated low-gravity match fairly well with true low-gravity. Further inspection of Figure 10(a) shows that the rate at which the interface location progresses through the domain significantly slows from full gravity $g/g_o = 1$ (natural convection) to $g/g_o = 10^{-1}$. The change is significantly less for the transition from $g/g_o = 10^{-1}$ to $g/g_o = 10^{-2}$, which suggests that a conduction-like processes is becoming evident. This is validated by superimposing the classical Stefan solution

$$(X_{\text{inf}} = \sqrt{2Ste\tau})$$

over the $g/g_o = 10^{-2}$ curve. Here it can be seen that both the classical Stefan solution and calculated interface location are nearly identical.

Figure 10(b) shows the results of varying Stefan number for the low-gravity case of $g/g_o = 10^{-2}$. It can be seen that both the magnetically and electromagnetically simulated low-gravity compare well with that of actual low-gravity for each value of Stefan. Furthermore, the classical Stefan solution has been superimposed over the results and shows good agreement with each value of Stefan.
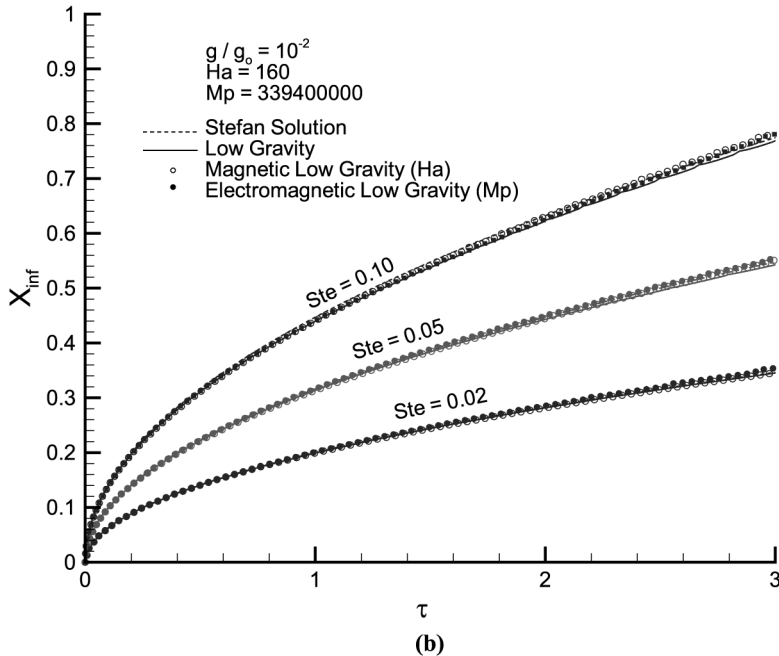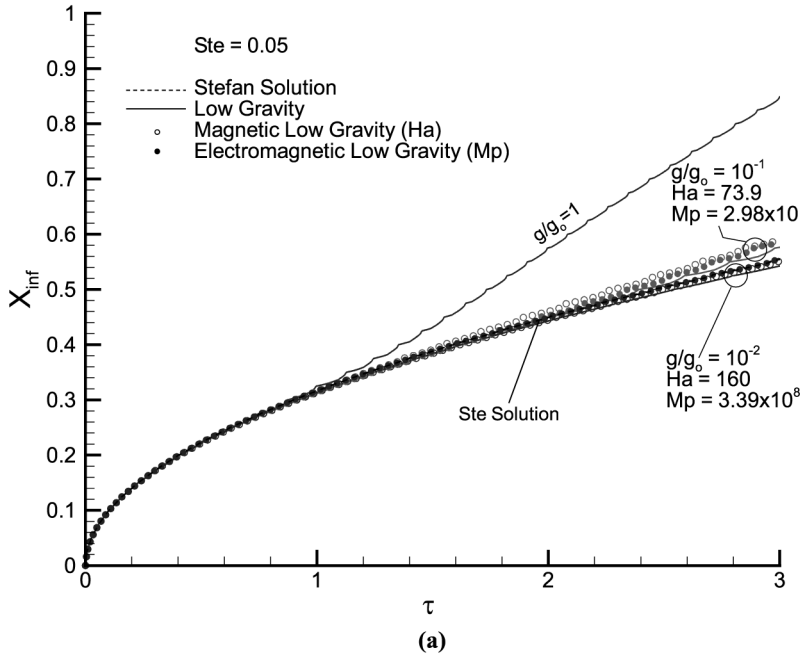
Melt rate
The ratio of solid PCM volume to its initial value (melt rate) is shown in Figure 11 as a function of dimensionless time. Figure 11(a) shows the effects of gravitational level on the melt rate, the results show that the melt rate for magnetically simulated low-gravity matches fairly well with actual low-gravity and also shows that the electromagnetically simulated low-gravity diverges with increased time. This can be explained by revisiting Figure 6, recall that two re-circulation cells existed for the electromagnetically simulated low-gravity case that were not present for actual low-gravity. These re-circulation cells caused the interface shape to vary from actual low-gravity and become slightly convex. As time increases these re-circulation cells develop in intensity causing more melting to occur and thus explains the diverging melt rate. Further inspection of Figure 10(a), shows that a significant decrease in the
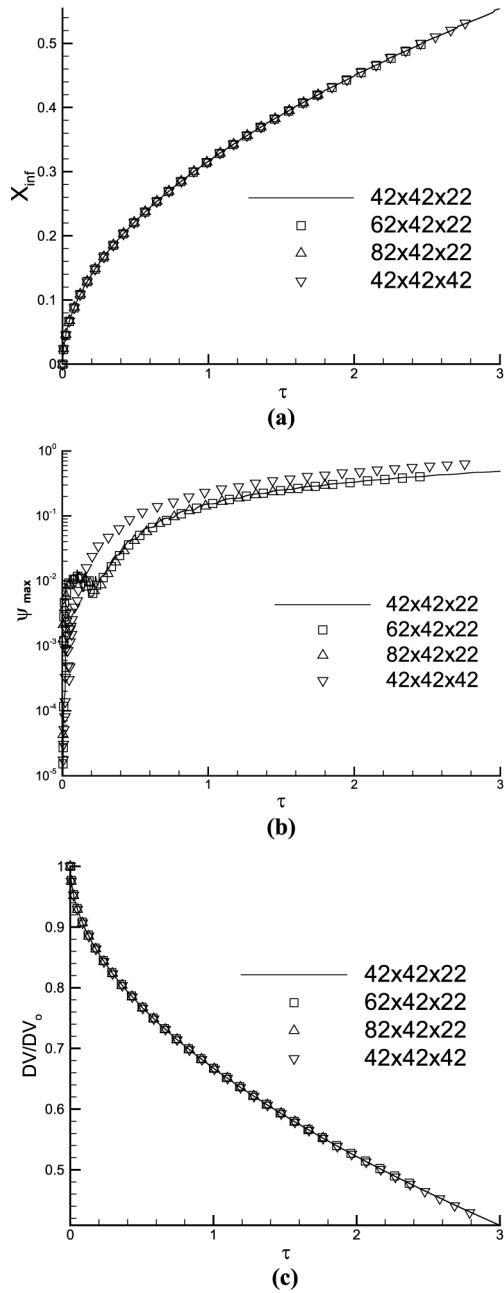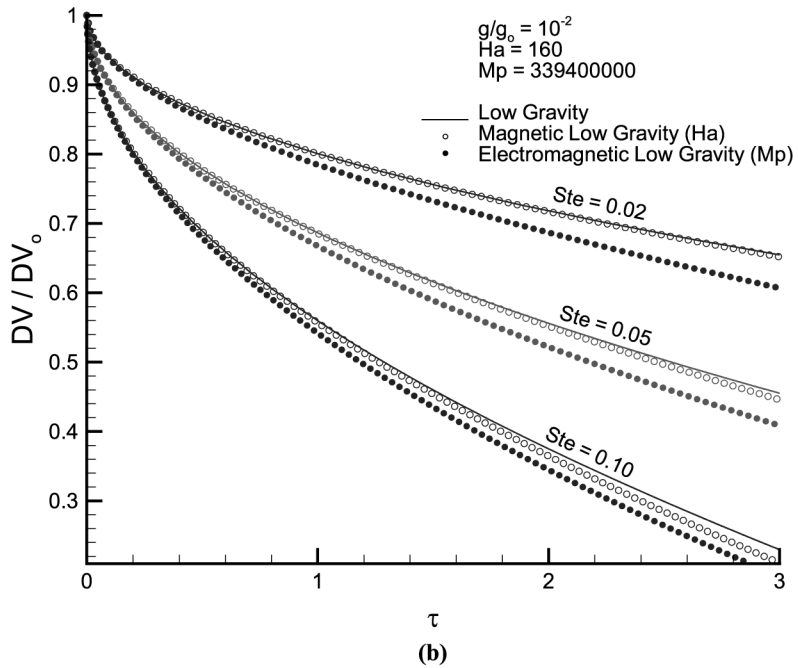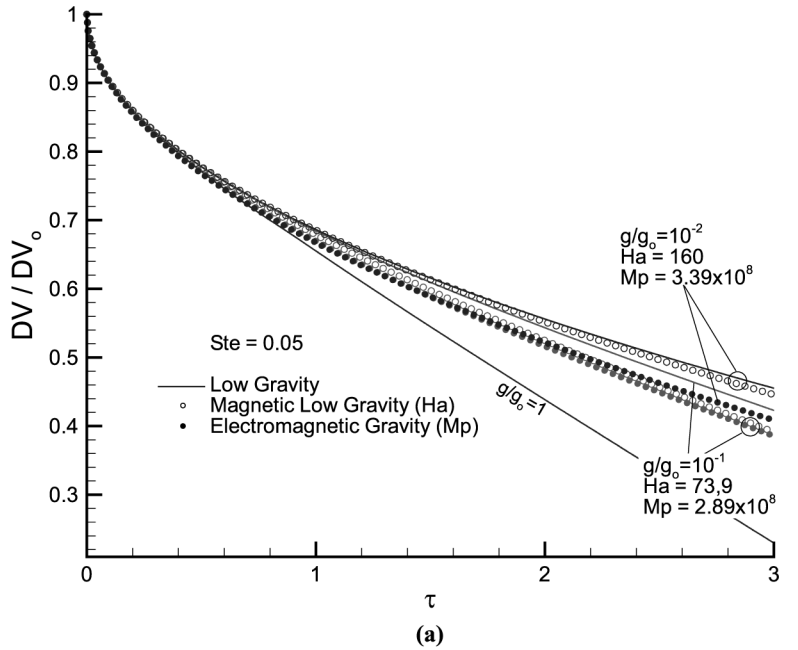
Figure 9.
Effect of grid density in
the *Z*-direction for
electromagnetically
simulated low-gravity
cases: (a) interface location
(X_{inf}), (b) mass circulation
(ψ_{max}), and (c) Melt rate

Ste = 0.05
-------- Stefan Solution
——— Low Gravity
∘ Magnetic Low Gravity (Ha)
• Electromagnetic Low Gravity (Mp)

$g/g_o = 10^{-1}$
Ha = 73.9
Mp = 2.98x10

$g/g_o = 1$

Ste Solution

$g/g_o = 10^{-2}$
Ha = 160
Mp = 3.39x10^8

(a)

$g / g_o = 10^{-2}$
Ha = 160
Mp = 339400000

-------- Stefan Solution
——— Low Gravity
∘ Magnetic Low Gravity (Ha)
• Electromagnetic Low Gravity (Mp)

Ste = 0.10

Ste = 0.05

Ste = 0.02

(b)

Figure 10.
Interface location in the X
direction (X_{inf}) as a
function of time: (a) effects
of gravity level, and (b)
effects of Stefan number

Figure 11.
Melt Rate as a function of time: (a) effects of gravity, and (b) effects of Stefan number (*Ste*)

melt rate occurs from full gravity $g/g_o = 1$ (natural convection) to $g/g_o = 10^{-1}$, which is in agreement with the behavior of the interface shape and interface location previously discussed.

The effect of varying Stefan number is shown in Figure 11(b). The results show that the melt rate agrees very well for magnetically simulated low-gravity for each value of Stefan examined. However, for the electromagnetically simulated low-gravity, the results again show a similar divergence with increasing dimensionless time. This divergence can be explained with the same reasoning as above for the varying gravity level case.
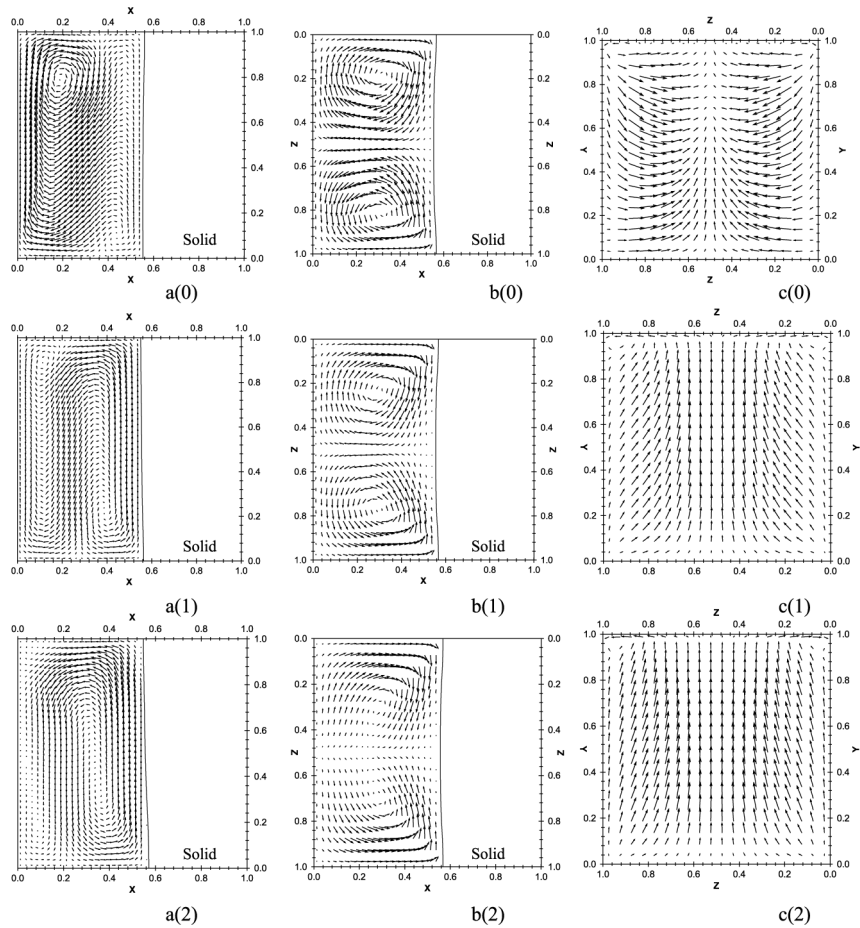
Flow reversal
A unique feature of simulating low-gravity via an electromagnetic field is a flow reversal phenomenon. Referring to Figure 4, this reversal can be seen quite clearly and occurs when the value of electromagnetic pressure exceeds the equivalent point of $Mp_e = 351130000.0$. Figure 12 shows the process occurring in three steps, where the labels (a), (b), and (c) represents the XY plane (at $Z = 0.5$), XZ plane (at $Y = 0.5$), and YZ plane (at $X = 0.5$), respectively. While labels 0, 1, and 2 represent the electromagnetically simulated low-gravity prior to reversal, at the equilibrium point and post-reversal, respectively. Essentially what is occurring is the Lorentz force, used to damp and or suppress the buoyancy forced created by the temperature gradient, is increasing to a point where it is larger than that of the buoyancy force.

This phenomenon can be readily explained if we revisit the source terms in the Y-momentum equation (equation (35)) pertaining to this behavior

$$(1 - f_s)GrPr^2\theta A + (1 - f_s)\frac{\Pi_{\Re}MpPr^2\theta A}{1 + \Pi_{\Re}\theta} \frac{\partial\psi}{\partial Z}$$

Both terms are a function of dimensionless temperature (θ) but behave the opposite of each other. Contributions by the Grashoff (Gr) or buoyancy term decreases in strength as θ decreases. However, the contribution of the electromagnetic pressure (Mp) term increases with decreasing values of (θ) because of the (θ) term in the denominator.

The flow prior to the equilibrium point is dominated by the buoyancy force ($Gr(\theta)$) and can be seen in Figures 12(a)(0)-(c)(0). Here two re-circulation cells are visible where the left cell or $Gr(\theta)$ cell can be seen to dominate over the right cell or Mp(θ). If you recall the flow field in Figure 5, there is one dominant clockwise re-circulation cell in the XY plane. But for this case, the effects of the $Gr(\theta)$ term are losing dominances over the flow field and the Lorentz force generated by the increasing electromagnetic field is approaching that of the buoyancy force. When the Lorentz force reaches the equivalent of the buoyancy force, "flow equilibrium" occurs (i.e. $Mp = Mp_e$). Here, neither the Lorentz or the buoyancy force dominates the flow which results in two near equivalent re-circulation cells (Figures 12(a)(1)-(c)(1)). The buoyancy force ($Gr(\theta)$ term) generates the left re-circulation and the right re-circulation is generated by the Lorentz force (Mp(θ) term). By further increasing the level of the electromagnetic field, the flow itself begins to revere in rotation. Figures 12(a)(2)-(c)(2) show this, it is clearly seen the re-circulation to the right (next to interface) is beginning to dominate the flow field. As the electromagnetic field is increased further the right re-circulation cell increases in intensity until fully over coming the left re-circulation cell and thus achieving full flow reversal without ever reaching zero.
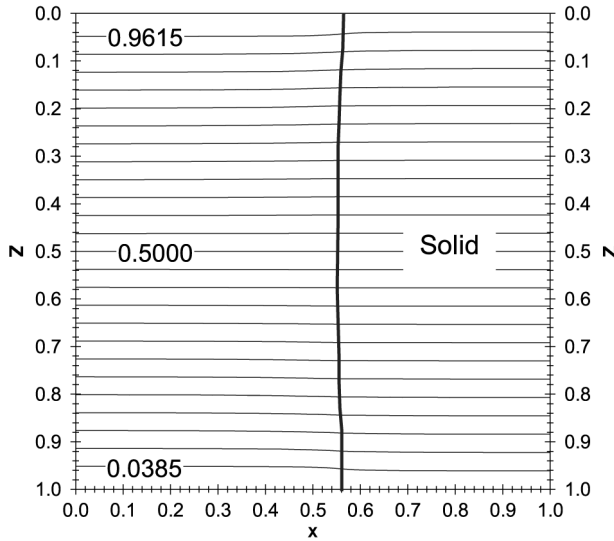
Figure 12.
Flow reversal interface
shape and velocity vector
field at $\tau = 3$ and
$Ste = 0.05$

Notes: (a) the XY Plane at Z = 0.5, (b) the XZ Plane at Y = 0.05,
(c) the YZ Plane at X = 0.05; (0) Prior to Flow reversal,
(1) Point of Flow Reversal, (2) Post Flow Reversal

Electric potential distribution
The electric potential distribution in the *XZ* plane can be seen in Figure 13 for the
$g/g_o = 10^{-2}$ electromagnetically simulated low-*g* case ($Mp = 3.39 \times 10^8$). The
electric potential distributions for all other levels of electromagnetic simulated low-*g*
follow in a similar fashion. Upon inspection of Figure 13, it can be seen that the
distribution is linear in the solid region but slightly non-linear in the liquid region
which can be seen by focusing attention to the electric potential lines at the
solid/liquid interface (bold line), where it can be seen change of phase causes a
slight "bend" to the electric potential lines. This behavior can be explained by
re-visiting equation (37) below

Notes: The bold line represents the solid/liquid
interface shape with the solid PCM to the right
on this line

$$\frac{\partial}{\partial X}\left(f_{\sigma(\Theta)}\frac{\partial \psi}{\partial X}\right) + \frac{\partial}{\partial Y}\left(f_{\sigma(\Theta)}\frac{\partial \psi}{\partial Y}\right) + \frac{\partial}{\partial Z}\left(f_{\sigma(\Theta)}\frac{\partial \psi}{\partial Z}\right)$$

$$= \frac{Ha^2}{\mathrm{Mp}Pr}\left[\frac{\partial}{\partial Y}(f_{\sigma(\Theta)}W) - \frac{\partial}{\partial Z}(f_{\sigma(\Theta)}V)\right]$$

the right hand side contains velocity gradients which explain the linear vs non-linear behavior of the electric potential. In the solid phase, these velocity gradients are equal to zero since the solid material is held fixed and $U = V = W = 0$. However, in the liquid phase these velocity gradients are present and contribute to the non-linearity of the electric potential distribution.

Two-dimensional vs three-dimensional comparison

As previously stated one of the objectives of this work was to extend the two-dimensional problem of Gonçalves *et al.* (2005) into three dimensions and assess the three-dimensional effects. Table V contains a comparison of all key parameter and results at $\tau = 3$ for both two- and three-dimensional problems. Comparison of these parameters shows that the values and results vary from one another by a significant percentage. It can be concluded that the two-dimensional solution provides only an approximation of the problem physics. The combination of the moving interface front and no slip conditions along the walls result in three-dimensional effects that cannot be ignore. These three-dimensional effects have been shown to influence the interface shape and flow field in ways not capture by only a two-dimensional analysis.

		$g/g_o = 10^{-1}$	$g/g_o = 10^{-2}$
Current work	Mp	289,000,000	342,500,000
Gonçalves *et al.* (2005)	Mp	237,610,000	264,050,000
	Δ percent	17.8 percent	22.2 percent
Current work	Ha	73.9	160
Gonçalves *et al.* (2005)	Ha	80.3	268
	Δ percent	7.9 percent	40.3 percent
Current work	ψ_{max}	2.2104	0.4889
Gonçalves *et al.* (2005)	ψ_{max}	1.9937	0.18428
	Δ percent	9.8 percent	62.3 percent
Current Work	X_{inf}	0.576	0.543
Gonçalves *et al.* (2005)	X_{inf}	0.620	0.550
	Δ percent	7.1 percent	1.4 percent
Current Work	DV/DV$_o$	0.423	0.543
Gonçalves *et al.* (2005)	DV/DV$_o$	0.340	0.380
	Δ percent	19.6 percent	30 percent

Table V.
Two-dimensional vs three-dimensional result comparison

Conclusions

The melting of a PCM by sidewall heating was utilized to study the effects of natural convection under actual low-gravity and electromagnetically simulated low-gravity. It was shown that the melting characteristics such as the maximum melt circulation, interface front location, and the melting rate under low-gravity environment can be simulated via magnetic and electromagnetic fields. However, the flow fields for magnetically simulated low-gravity show significant distortion from that of actual low-gravity. While for the case of electromagnetically simulated low-gravity, good agreement of the flow field can be found only in the *XY* plane. The two remaining planes show distortions in the flow field but the overall effect appears to be minimal on the studied parameters. Furthermore, it was also shown that when the level of gravity is reduced by two orders of magnitude the melting process becomes conduction-like. It was further shown that under electromagnetic simulation, it is possible to achieve flow reversal for Mp greater than a certain critical value, Mp$_e$. Finally, it was learned that the flow reversal was accompanied by a transition mechanism that allow the convection process to be either thermally or electromagnetically dominated, but never completely halted.

In closing, the electromagnetic simulation of low-gravity allows the flow field distortion due to high magnetic field to be significantly reduced and thereby more accurately simulate the effects of actual low-gravity.

References

Asako, Y., Gonçalves, E., Faghri, M. and Charmchi, M. (2002), "Numerical solution of melting processes for fixed and unfixed phase change material in the presence of electromagnetic field – simulation of low gravity environment", *Numerical Heat Transfer, Part A*, Vol. 42, pp. 565-83.

Asako, Y. and Faghri, M. (1999), "Effect of density change on melting of unfixed rectangular phase-change material under low-gravity environment", *Numerical Heat Transfer, Part A*, Vol. 36, pp. 825-38.

Bessaih, R., Kadja, M. and Marty, Ph. (1999), "Effect of wall electrical conductivity and magnetic field orientation on liquid metal flow in a geometry similar to the horizontal Bridgman

configuration for crystal growth", *International Journal of Heat and Mass Transfer*,
Vol. 42, pp. 4345-62.

Cao, Y. and Faghri, A. (1989), "A numerical analysis of Stefan problems for generalized
multi-dimensional phase-change structures using the enthalpy transforming model",
International Journal of Heat Mass Transfer, Vol. 32 No. 7, pp. 1289-98.

Davidson, P.A. (2001), *Introduction to Magnetohydrodynamics*, Cambridge University Press,
Cambridge, MA.

Dennis, B. and Dulikravich, G. (2002), "Magnetic field suppression of melt flow in crystal
growth", *International Journal of Heat and Fluid Flow*, Vol. 23, pp. 269-77.

Dulikravich, G. and Kosovic, B. (1992), "Solidification of variable property melts under the
influence of low gravity, magnetic fields and electric fields", AIAA paper 92-0694, AIAA
Aerospace Sciences Meeting, Reno, NV, 6-9 January.

Dulikravich, G., Ahuja, V. and Lee, S. (1994), "Modeling three-dimensional solidification with
magnetic fields and reduced gravity", *International Journal of Heat and Mass Transfer*,
Vol. 37 No. 5, pp. 837-53.

Filyand, M.A. and Semenova, E.I. (1968), *Handbook of the Rare Elements I: Trace Elements and
Light Elements*, 1st ed., Boston Technical Publishers, Boston, MA.

Gonçalves, E., Faghri, M., Asako, Y. and Charmchi, M. (2005), "Numerical solution of melting in
side-heated rectangular enclosure under electromagnetically simulated low gravity",
Numerical Heat Transfer, Part A, Vol. 47 No. 4, pp. 315-32.

Ha, M., Lee, H. and Seong, S. (2003), "Numerical simulation of three-dimensional flow, heat
transfer, and solidification of steel in continuous casting mold with electromagnetic
brake", *Journal of Materials Processing Technology*, Vol. 133, pp. 322-39.

Harada, H., Takeuchi, E., Zeze, M. and Tanaka, H. (1998), "MHD analysis in hydromagnetic
casting process of clad steel slabs", *Applied Mathematical Modeling*, Vol. 22, pp. 873-82.

Hayase, T., Humphrey, J.A.C. and Greif, R. (1992), "A consistently formulated QUICK scheme for
fast and stable convergence using finite-volume iterative calculation procedures", *Journal
of Computational Physics*, Vol. 98, pp. 108-18.

Metals Handbook (1990), *Properties and Selection: Nonferrous Alloys and Special-Purpose
Materials*, 10th ed., Vol. 2, ASM International, Chicago, IL, pp. 1114-5.

Ozoe, H. and Okada, K. (1989), "The effect of the direction of the external magnetic field on the
three-dimensional natural convection in a cubical enclosure", *International Journal of Heat
Mass Transfer*, Vol. 32 No. 10, pp. 1939-54.

Patankar, S.V. (1980), *Numerical Heat Transfer and Fluid Flow*, Hemisphere Publishing,
New York, NY.

Ramo *et al.* (1994), *Field and Waves in Communication Electronics*, Wiley, New York, NY.

Yahia, J. and Thobe, J.P. (1972), "Temperature Dependence of the Resistivity of Liquid Gallium to
1,000°C", *Canadian Journal of Physics*, Vol. 50 No. 20, pp. 2554-6.